High-Surface-Area Mesoporous Activated Carbon from Hemp Bast Fiber Using Hydrothermal Processing

Md Zakir Hossain [ID], **Wei Wu, William Z. Xu, Muhammad B. I. Chowdhury, Anil Kumar Jhawar, Devin Machin and Paul A. Charpentier ***

Department of Chemical and Biochemical Engineering, The University of Western Ontario, London, ON N6A 5B9, Canada; mhossa32@uwo.ca (M.Z.H.); wwu222@uwo.ca (W.W.); zxu27@uwo.ca (W.Z.X.); mchowdh4@uwo.ca (M.B.I.C.); ajhawar2@uwo.ca (A.K.J.); dmachin@uwo.ca (D.M.)

* Correspondence: pcharpentier@eng.uwo.ca; Tel.: +1-(519)-661-3466

Abstract: Synthesis of activated carbon from waste biomass is of current interest towards sustainability. The properties of biomass-derived activated carbon largely depend on the carbonization process. This study reports the preparation of mesoporous activated carbon with extremely high surface area from hemp bast fiber using hydrothermal processing. Hot water processing (390–500 °C) followed by activation using KOH and NaOH was investigated at different mass ratios. The described approach was found to enhance the mesoporosity (centered at 3.0 to 4.5 nm) of the hemp-derived activated carbon (HAC) from activation [confirmed by BJH (Barrett-Joyner-Halenda) pore size distribution and TEM (transmission electron microscopy) imaging]. BET (Brunauer-Emmett-Teller) results showed that the product has an extremely high surface area (2425 m^2/g) while the surface functional groups (–OH, –COOH, C=C/C–C) were confirmed by FTIR (Fourier transform infrared spectroscopy) and further quantified by XPS (X-ray photoelectron spectroscopy). Increasing KOH concentration was found to enhance the surface area with a maximum biochar-to-KOH (g/g) ratio of 1:3. The crystallite domain size of HAC was determined using Raman spectroscopy of different wavelengths. The procedure described in this study is an environmentally friendly scalable route for the mass production of activated carbon using hemp fiber.

Keywords: hemp bast fiber; hydrothermal processing; KOH activation; activated carbon

1. Introduction

Activated carbon is a well-known porous material with large surface area and pore volume, and is extensively used for gas separation, solvent recovery, contaminant removal from water, wastewater treatment, and as a catalyst/catalyst support for different energy storage and conversion processes [1]. Recently, activated carbon has been extensively investigated for making carbon foams [2] and ultracapacitors/supercapacitors [3,4] due to its porous structure. As the pore properties of activated carbon largely depend on the precursor materials and the synthesis method, different types of materials (natural and synthetic) have been examined as precursors. The most commonly used precursors for activated carbon production are coal, coconut shell, wood, agricultural wastes, or industrial wastes [1]. Among them, biomass as a precursor is attracting significant attention as it is renewable, abundant, low cost, and eco-friendly.

Two basic activation processes, i.e., physical and chemical, are used to prepare activated carbonaceous materials from biomass [5]. Prior to either the physical or chemical activation process, the carbon precursor needs to be carbonized to produce char. If the formed char is activated using

carbon dioxide or steam as the activating agent, the process is called physical activation [6]. If the char is activated in the presence of chemical agents, the process is termed chemical activation [7]. The step for char production can occasionally be skipped if chemical activation is employed. To obtain a well-developed pore structure in the final carbon product using physical activation, a significant amount of internal carbon mass removal is necessary. Activating agents used for chemical activation are dehydrating agents that enhance pyrolytic decomposition and prevent tar formation, thus enhancing the yield of carbon [5]. The most commonly used agents for chemical activation are acidic reagents such as $ZnCl_2$, H_3PO_4, HCl, and H_2SO_4 or the basic reagents KOH, K_2CO_3, NaOH, and Na_2CO_3. There is a growing interest in using alkali hydroxides as the activation agent, with KOH being one of the most promising activating agents [8,9]. In this work, KOH and NaOH are compared as activating agents while hemp bast fiber was chosen as the carbon precursor because of its unique fibrous structure to make carbonaceous materials [10]. Hemp has been used for various applications such as rod, sails, clothing, paper, building materials, food, medicine, oil, fuel, and in the plastic industry [11], with carbonized hemp fiber being studied by several research groups [11–13]. Wang et al. [11] used sulphuric acid solution in their process to prepare carbon material from hemp fiber whereas Yang et al. [12] and Rosas et al. [13] conducted the carbonization reaction in the presence of phosphoric acid. Using acid for this carbonization process provides an acid disposal issue after the reaction. Hydrothermal processing of hemp bast fiber followed by chemical activation can be an alternative approach for making carbon materials.

Detailed structural and surface properties are very important for the application of the resultant product. The current study synthesizes hemp-derived carbon materials and characterizes them in detail by various physicochemical techniques including BET (Brunauer-Emmett-Teller) surface area and BJH (Barrett-Joyner-Halenda) pore size distribution, XRD (X-ray powder diffraction), SEM (scanning electron microscopy), TEM (transmission electron microscopy), Raman, TG-DTA (thermogravimetric & differential thermal analysis, FTIR (Fourier transform infrared spectroscopy), and XPS (X-ray photoelectron spectroscopy) analysis.

2. Materials and Methods

2.1. Materials

Hemp bast fiber was purchased from American Hemp, Winston Salem, NC, USA. KOH, NaOH, and 36% to 40% HCl were obtained from Caledon Laboratories Ltd., Georgetown, ON, Canada. Silica-alumina pellets were obtained from Micromeritics Instrument Corporation, Norcross, GA, USA. Powdered activated carbon (DARCO G-60, 100−325 mesh particle size) and Basolite® C300 were obtained from Sigma Aldrich Canada Co., Oakville, ON, Canada. Activated carbon Norit Row 0.8 mm pellets (steam activated) were obtained from Alfa Aesar, Tewksbury, MA, USA. Deionized (DI) water (18.2 MΩ) was taken from a compact ultrapure water system (EASY pure LF, Mandel Scientific Co., Guelph, ON, Canada, model BDI-D7381).

2.2. Preparation of Hemp-Derived Activated Carbon (HAC)

A quantity of 200 mL of DI water along with 12.0 g of pre-cut hemp bast fiber were sealed in a 600 mL Hastelloy C-276 reactor (Autoclave Engineers, Erie, PA, USA), heated to the desired temperature (390 °C, 450 °C, or 500 °C), and kept for 2 h. The resultant biochar was recovered by vacuum filtration and washed with DI water multiple times, then dried overnight at 120 °C in a vacuum oven. The dried biochar was thoroughly mixed with a preset amount of KOH or NaOH (wt ratios of biochar to KOH or NaOH: 1:1, 1:2, and 1:3) using a mortar and pestle, then heated to 750 °C (0.5 °C/min) and kept at 750 °C for 1 h under Argon flow in a tubular furnace. The resulting product was thoroughly washed with 20% HCl followed by DI water until pH 7.0 was reached. Finally, the products were dried overnight at 120 °C in a vacuum oven. Activation of biochar using KOH to

produce the final product was repeated at least three times. The yields of final products were 59%, 65%, and 71% when using biochar-to-KOH ratios of 1:3, 1:2, and 1:1, respectively.

2.3. Instrumentation

The Brunauer–Emmett–Teller (BET) surface area, pore diameter, and pore volume of hemp-derived activated carbon (HAC) and biochar were determined from nitrogen adsorption and desorption isotherm data obtained at −196 °C in a constant-volume adsorption apparatus (Tristar II 3020, Micromeritics Instrument Corporation, Norcross, GA, USA) using 99.995% pure N_2 gas obtained from Praxair (Oakville, ON, Canada). The prepared samples were degassed at 130 °C for 12 h to remove any moisture and other adsorbed gases from the surface. The pore size distributions were calculated using the BJH (Barrett-Joyner-Halenda) method from the desorption branch of the isotherms. The instrument calibration was examined by using the standard (silica-alumina pellets) obtained from the instrument supplier (Micromeritics Instrument Corporation, Norcross, GA, USA). Calibration was also checked by using commercial activated carbons and Basolite where their specific surface areas are known. Details about the calibration results are provided in the Supplementary Materials (Table S1).

X-ray diffraction (XRD) measurements were performed using a Bruker D2 PHASER desktop diffractometer (Madison, WI, USA) using Cu Kα radiation (1.54 Å). The instrument was operated at 30 kV and 10 mA, using a scan rate of 0.1° per second in the 2θ range from 10° to 70°. The morphology of the HAC was obtained using Scanning Electron Microscopy (SEM) (Hitachi FlexSEM, model SU 1000) (Schaumburg, IL, USA) with a secondary electron detector and Transmission Electron Microscopy (TEM) (model JEOL 2010F) (Peabody, MA, USA). The X-ray photoelectron spectroscopy (XPS) analysis was carried out with a Kratos Axis Ultra spectrometer (Kratos Analytical Ltd., Manchester, UK) using a monochromatic Al Kα source (15 mA, 14 kV). FTIR (Fourier transform infrared) analyses of the hemp-derived samples were examined using an ATR–FTIR spectroscope (Nicolet 6700 FTIR) (ThermoFisher Scientific, Waltham, MA, USA). Raman spectroscopy measurements were performed using a Kaiser Optical Systems RXNI-785 (Ann Arbor, MI, USA) with an excitation wavelength of 785 nm. Crystallite domain sizes of the AC catalysts were measured using a Renishaw InVia Reflex Raman spectrometer (New Mills, Gloucestershire, UK) with two additional wavelength lasers (633 nm and 514 nm). Thermogravimetric and differential thermal analysis (TG-DTA) was conducted on a TA Q600 system (New Castle, DE, USA) with a heating rate of 10 °C/min from ambient temperature to 1000 °C in N_2 with a flow rate of 50 mL/min.

3. Results

Textural properties are critical for optimizing the application of any porous material. Textural properties of prepared HAC using hydrothermal processing are listed in Table 1, where the average values are reported after measuring three times. It is seen that the HAC obtained very high surface area once activated by KOH or NaOH. KOH demonstrated advantages over NaOH in pore development of biochar. Both the BET and Langmuir surface areas slightly increase with increasing biochar synthesis temperature from 390 °C to 500 °C. Generally, the pore volume and pore size of the final product were found to be insensitive to the biochar synthesis temperature.

Table 2 compares the BET surface areas of activated carbon obtained in the present study with those obtained using different feedstocks/activating reagents reported in the literature, with the present study showing the highest BET surface area of 2425 m^2/g. It is generally believed that the KOH activation process of any carbon material enhances the pore structure and morphology with a substantial increase in specific surface area [14].

Table 1. Pore properties of hemp-derived activated carbon (HAC).

Sample	Biochar Synthesis Temperature (°C)	Activating Reagent	Weight Ratio of Biochar and Activating Reagent	BET Surface Area (m²/g)	Langmuir Surface Area (m²/g)	Pore Volume (cm³/g)	Average Pore Size (nm)
Hemp-Derived Biochar	–	–	–	2	3	0.001	–
HAC	390	KOH	1:1	1566	2078	0.810	4.6
	450	KOH	1:1	1587	2090	0.811	4.6
	500	KOH	1:1	1598	2101	0.813	4.6
	390	KOH	1:2	1992	2647	1.011	4.3
	390	KOH	1:3	2425	3363	1.216	2.9
	390	NaOH	1:1	1252	1673	0.662	4.3
	390	NaOH	1:2	1851	2525	0.925	3.1
	390	NaOH	1:3	2124	2848	1.017	2.9

Table 2. BET surface areas of activated carbons prepared from different sources of biomass as feedstocks.

Biomass Feedstocks	Activator Used	BET Surface Area (m²/g)
Walnut shell [15]	CO_2	379
Sunflower stem [15]	CO_2	438
Olive stone [15]	CO_2	438
Rice husk [16]	CO_2	446
Glucose/ovalbumin [17]	–	476
Pinewood [16]	CO_2	569
Glucose/borax [18]	–	614
Orange peel [19]	CO_2	618
Glucose [20]	KOH	1197
Palm date seed [21]	NaOH	1282
Desert shrub [22]	$ZnCl_2$	1296
Rice husk [23]	H_3PO_4	1498
Hazelnut shell [24]	KOH	1700
Glucose [25]	KOH	1704
Sucrose [26]	H_3PO_4	2120
Glucose [26]	NaOH	2129
Starch [27]	KOH	2190
Rye straw [28]	KOH	2200
Eucalyptus sawdust [29]	KOH	2252
Corncobs [30]	KOH	2300
Hemp bast fiber (this study)	KOH	2425

Figure 1 provides the N_2 adsorption–desorption isotherms at −196 °C and pore size distributions of HAC, where HACs were prepared using different biochar-to-KOH ratios at a synthesis temperature of 390 °C. All the adsorption–desorption isotherms exhibit a type IV isotherm with a type IV hysteresis loop (according to IUPAC classification) in the relative pressure range from 0.4 to 1.0. Type IV isotherms are an indication of the existence of well-developed mesopores in the structure, whereas a type IV hysteresis loop indicates the formation of asymmetric, slit-shaped mesopores, attributable to rapid gas evolution and open channels [31]. It has been observed that increasing the ratio of activating agent to biochar increases the textural properties (surface area and pore volume) significantly, attributed to increasing the etching effect of the activating reagent on the biochar surface, thus creating mesopores from micropores [32]. The unique mesoporous structure of HAC contributes to the high specific surface area and uniform pore size distribution. The activation temperature also plays an important role in improving the specific surface area and pore volume. High-temperature activation was shown to enhance porosity as previously confirmed by Wang et al. [11], while low temperatures were not favorable to increasing porosity due to the low reaction rate between the activator and carbonaceous material. Wang et al. [11] obtained the highest BET surface area (2287 m²/g) for making interconnected carbon nanosheets at 750 °C during the activation of biochar with KOH.

The pore size distributions (PSD) of HAC prepared using different biochar-to-KOH ratios show that all the samples have a very narrow pore size distribution, mainly centered at 3.0 to 4.5 nm. This result is intriguing and indicates highly mesoporous carbon formation. Foo and Hameed [33] reported an average pore size of 21.44 nm in activated carbon produced from pistachio nut shells via microwave-induced chemical (KOH) activation. The same authors [34] also reported average pore sizes of 34.14 nm and 26.89 nm for activated carbon from rice husk as a feedstock using KOH and K_2CO_3 activation. Tay et al. [7] synthesized different types of activated carbon from soybean oil cake and reported an average pore diameter of 5.23 nm in one of the products.
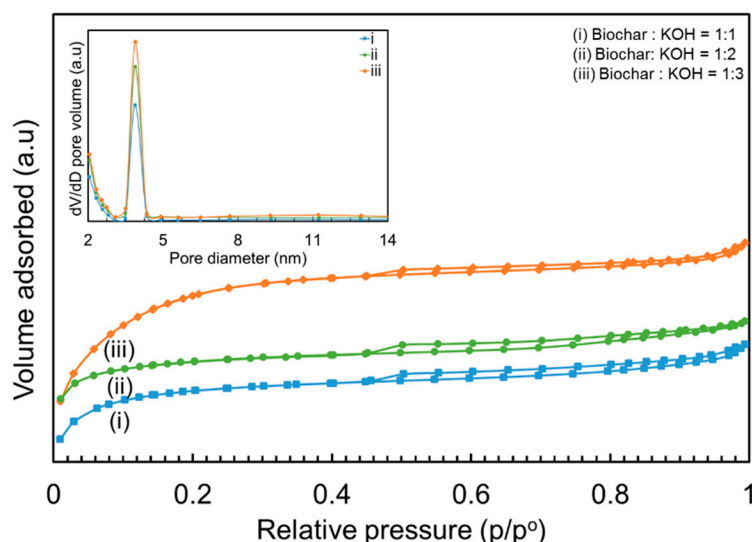
Figure 1. Nitrogen adsorption–desorption isotherms and BJH (Barrett-Joyner-Halenda) pore size distributions of HAC (inset).

The morphology of a material is a crucial factor for its application. The morphology of HAC was investigated and is presented in Figures 2 and 3. Figure 2 shows the SEM images of the obtained hemp biochar (a) and HAC using different ratios of biochar to KOH at 1:1 (b), 1:2 (c), and 1:3 (d). The observed HAC surface morphologies are very different to those from biochar. The biochar surface is rough with irregular sizes of particles and many large defect holes whereas the HAC surface shows the amorphous nature of carbon with a large mesopore content. The differences in morphologies among Figure 2b–d suggest that KOH plays an important role in pore development of the resultant samples during activation. Figure 3a shows the TEM image of biochar whereas Figure 3b–d show the resulting HAC using different KOH ratios. Biochar does not have any pores whereas the activated carbon obtained using different biochar/KOH ratios have a regular porous structure. The TEM and SEM images corroborate the BET results. Lu et al. [35] found a similar mesoporous structure (adsorption average pore width = 3.23 nm) in activated carbon synthesized from corn straw. The high surface area and mesoporosity of HAC will be useful for gas storage and adsorption applications, and for making carbon foam, supercapacitors, or ultracapacitors, etc., by providing more active sites.
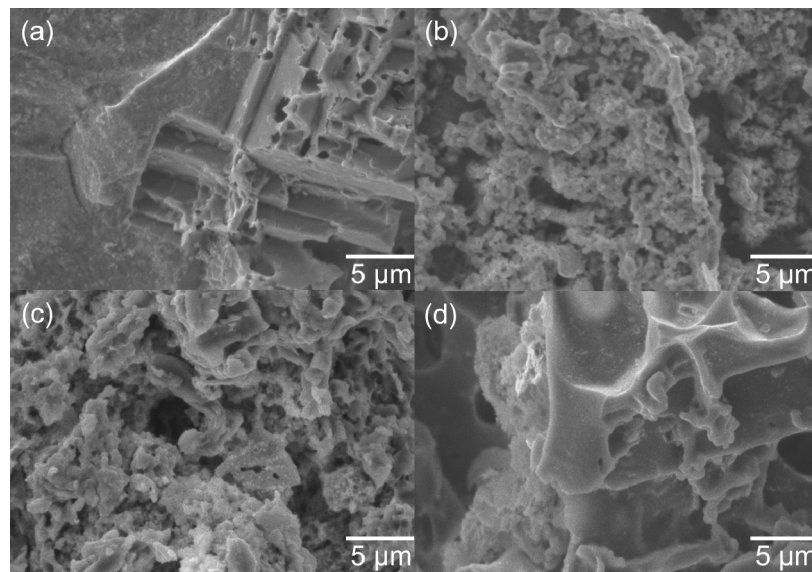
Figure 2. SEM (scanning electron microscopy) images of (**a**) obtained biochar and HAC obtained using different ratios of biochar to KOH ((**b**) 1:1; (**c**) 1:2; (**d**) 1:3).
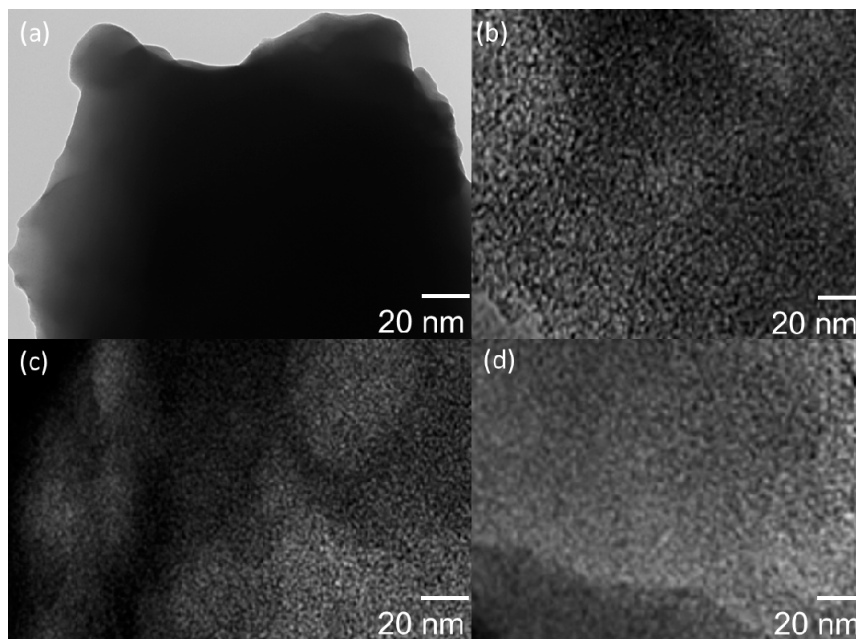

Figure 3. TEM (transmission electron microscopy) images of (**a**) biochar and HAC obtained using different ratios of biochar to KOH ((**b**) 1:1; (**c**) 1:2; (**d**) 1:3).

X-ray diffraction (XRD) was used to determine the crystalline structure of HAC. Figure 4 shows the small- and large-angle XRD patterns for the HAC samples. The small-angle XRD pattern for all three samples indicates the formation of an ordered hexagonal mesoporous structure [36]. This type of small-angle XRD peak is completely absent in commercial activated carbon, indicating the lack of a long-range porous structure [37]. The large peak at 23.4° 2θ (C(002)) in Figure 4 corresponds to the amorphous carbon structure. The weak and broad C(100) peak at 2θ = 40–50° is attributed to the *a* axis of the graphite structure [38]. The XRD patterns for all three investigated samples are very similar. This suggests that the different ratios of activating agent and biochar do not have a noticeable effect on

the structural changes of HAC. Similar large-angle XRD patterns were reported by Lu et al. [35] for the synthesis of mesoporous activated carbon from waste biomass material such as corn straw.

The HAC samples were characterized by FTIR (Fourier transform infrared), with the spectra shown in Figure 5. According to the literature [39], the peak at 3288 cm^{-1} is attributed to O–H stretching while the peaks at 2977 cm^{-1}, 2941 cm^{-1}, 2914 cm^{-1}, and 2830 cm^{-1} are ascribed to asymmetric CH_3, asymmetric CH_2, symmetric CH_3, and symmetric CH_2 stretching modes. The peak at 1447 cm^{-1} is attributable to CH_2 scissoring and CH_3 asymmetric bending modes. The peak at 1402 cm^{-1} can be assigned to O–H in-plane bending and CH_3 umbrella modes. The peak at 1109 cm^{-1} is attributable to CH_3 rocking or CH_2 wagging modes. The peak at 1016 cm^{-1} is mainly attributed to alcoholic C–O stretching mode. No significant difference is observed among the spectra of these samples, suggesting similar surface functional groups regardless of the biochar-to-KOH ratio. The presence of such functional groups was also reported by Barkauskas et al. [40] for commercial granulated activated carbon.

Raman spectroscopy was used to examine the ordered and disordered crystal structures of the HAC. Figure 6 compares the Raman spectra of hemp-derived activated carbon samples collected using a 785 nm laser. In these spectra, the G band at 1588 cm^{-1} corresponds to the first-order scattering of E_{2g} mode and is related to the vibration of sp^2-bonded carbon atoms. The D band at 1315 cm^{-1} arises from a breathing mode of *k*-point phonons of A_{1g} symmetry [41]. The D band corresponds to the amount of disorder and its intensity shows a degree of edge chirality [42]. By deconvoluting these peaks, the intensity ratios of D/G (I_D/I_G) were calculated and are listed in Table 3. The samples from the ratios of biochar to KOH at 1:1 and 1:2 demonstrated the same intensity ratio (I_D/I_G) of 1.37, which is lower than that (1.44) obtained from the ratio of biochar to KOH at 1:3. High I_D/I_G ratios suggest a high level of disorder such as defects, ripples, and edges [43]. Besides this, the full width at half-maximum (FWHM) of the G band (Γ_G) increased from 92.8 cm^{-1} to 111.7 cm^{-1} when the ratio of biochar to KOH decreased from 1:1 to 1:3. As reviewed by Maslova et al. [44], higher Γ_G represents a larger amount of defects for carbonaceous materials.
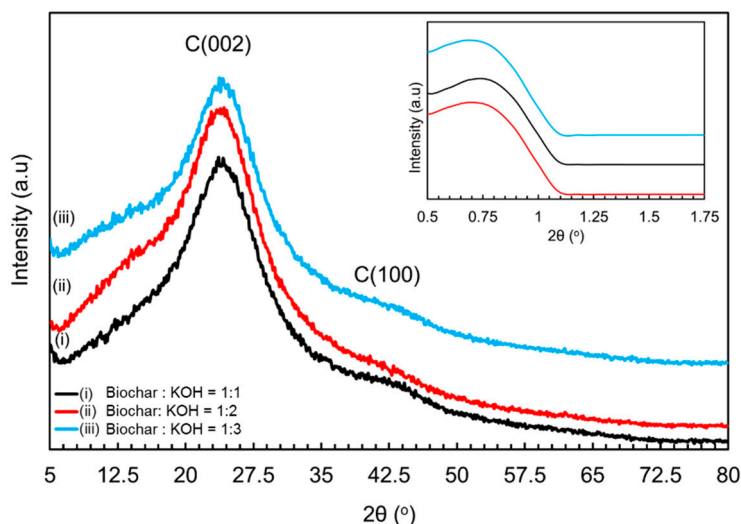

Figure 4. Large-angle and small-angle (inset) XRD patterns of the HAC.
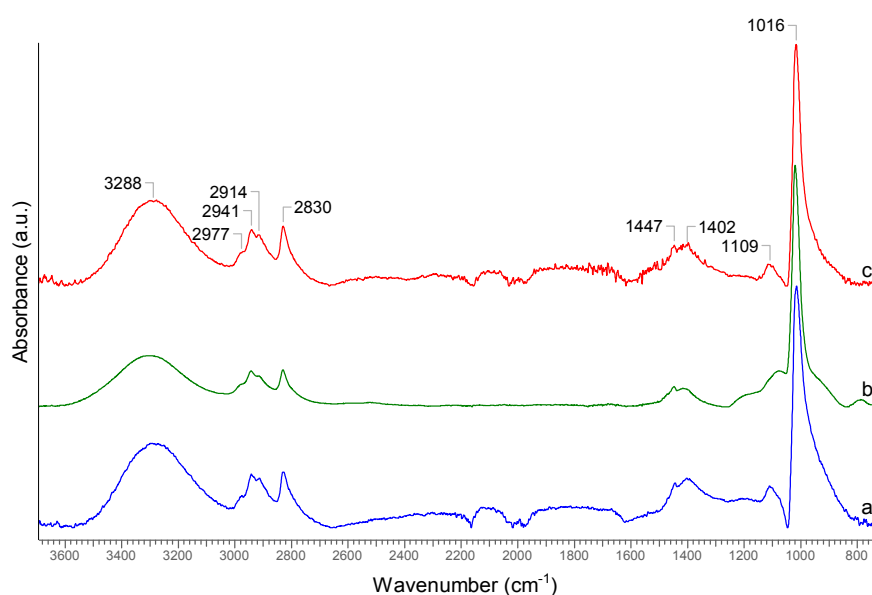
Figure 5. ATR–FTIR (Attenuated total reflectance-Fourier transform infrared) spectra of hemp-derived activated carbon at different biochar and KOH ratios ((a) 1:1, (b) 1:2, and (c) 1:3).

It has been reported that the crystallite domain size (La) of carbonaceous materials can be calculated using the equation $La = C(\lambda_L)/(I_D/I_G)$ where a linear relationship $C(\lambda_L) \approx C_0 + \lambda_L C_1$ is valid in the excitation wavelength range of 400 nm < λ_L < 700 nm where $C_0 = -12.6$ nm and $C_1 = 0.033$ [45]. In order to study the domain size of the HAC samples, the Raman spectra of these samples were also collected using two other laser sources with respective wavelengths of 633 nm and 514 nm. The I_D/I_G and La values were calculated and are listed in Table 3. According to these results, the domain sizes of the samples obtained from biochar to KOH ratios of 1:1 and 1:2 are similar, but larger than those obtained using a biochar-to-KOH ratio of 1:3. These results are in good agreement with the Raman results measured using the 785 nm laser, i.e., the crystallite domain size did not change much when the ratio of biochar to KOH changed from 1:1 to 1:2, but decreased when the ratio of biochar to KOH changed to 1:3.
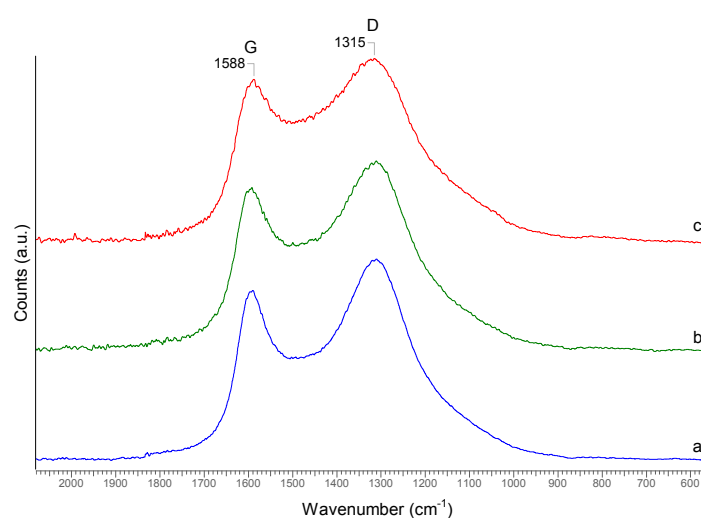

Figure 6. Raman spectra of hemp-derived activated carbon at different biochar and KOH ratios ((a) 1:1, (b) 1:2, and (c) 1:3).

Table 3. Raman results of the HAC samples obtained from different biochar-to-KOH ratios.

Ratios	λ = 785 nm		λ = 633 nm		λ = 514 nm	
	I_D/I_G	Γ_G (cm^{-1})	I_D/I_G	La (nm)	I_D/I_G	La (nm)
1:1	1.37	92.8	1.112 ± 0.007	7.46 ± 0.05	1.008 ± 0.043	4.33 ± 0.18
1:2	1.37	102.2	1.105 ± 0.035	7.50 ± 0.24	1.028 ± 0.017	4.24 ± 0.07
1:3	1.44	111.7	1.191 ± 0.016	6.96 ± 0.09	1.071 ± 0.020	4.07 ± 0.08

The surface chemistry of HAC was characterized using X-ray photoelectron spectroscopy (XPS). XPS survey spectra of HACs are summarized in Figure 7a and Table 4. Figure 7a and Table 4 show that increasing the biochar-to-KOH ratio increases the atomic percentages of O (from 16.6% to 24.2%) and decreases the atomic percentages of C (80% to 70.7%). Similar trends were confirmed by Tai et al. [46] for synthesizing activated carbon from graphite using different KOH ratios. The atomic percentage of Si also slightly increased (from 2.3% to 4.2%) with increasing ratios. Si is the second most abundant element in soils which is found in substantial amounts in many plants [47]. Higher amounts of KOH helped to precipitate higher Si on the surface of HAC.
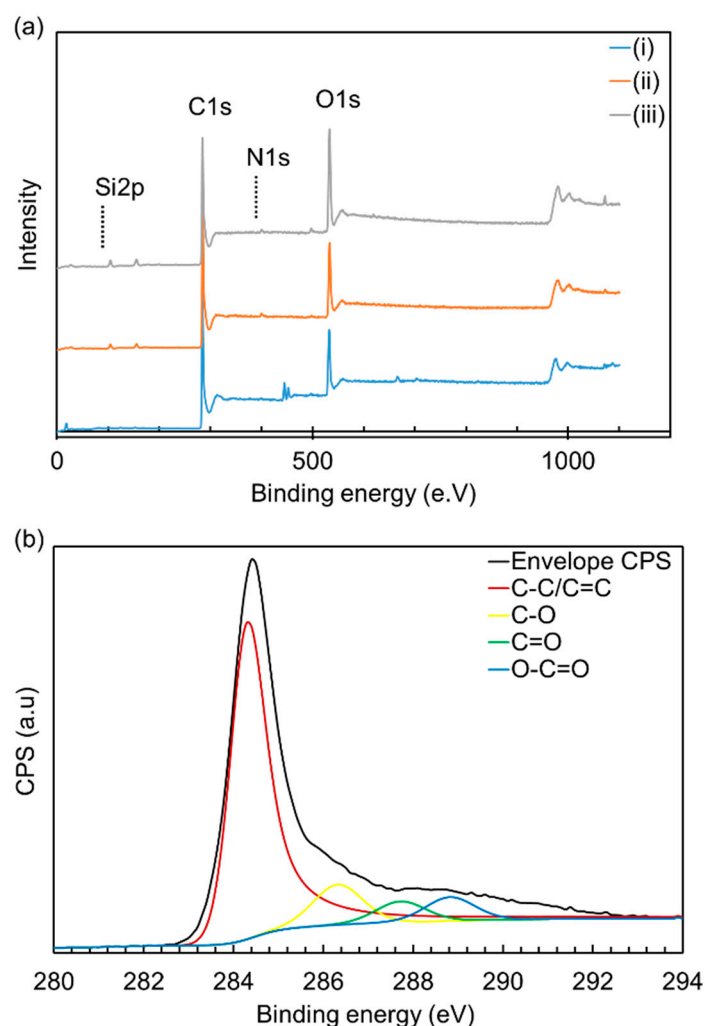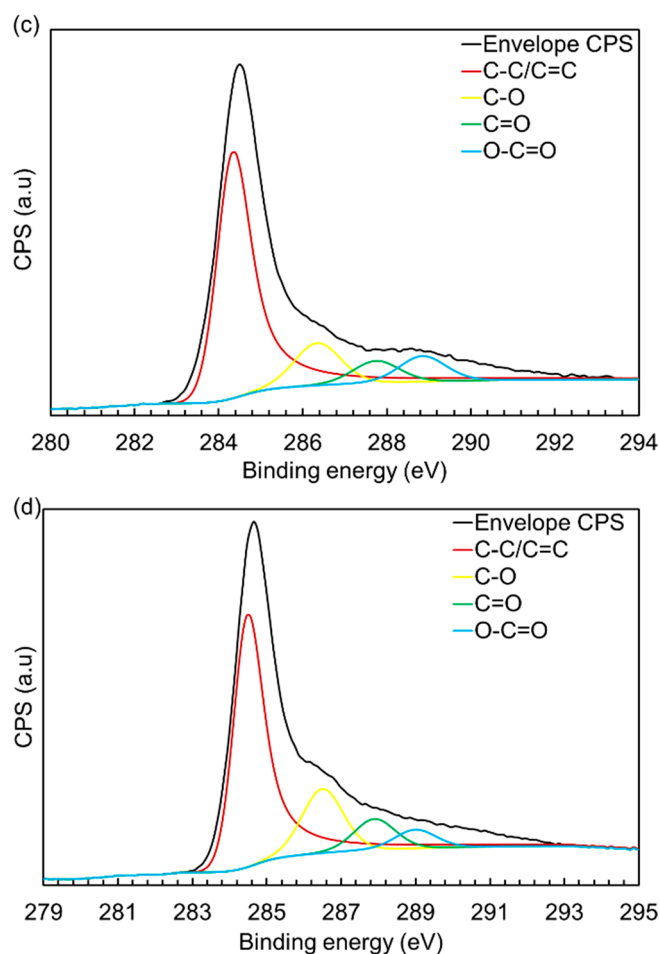

Figure 7. *Cont.*

Figure 7. (**a**) XPS survey spectra of HAC obtained using different ratios of biochar to KOH. (i) 1:1; (ii) 1:2; (iii) 1:3. High-resolution C(1s) XPS spectra of resultant HAC obtained using different ratios of biochar to KOH. (**b**) 1:1; (**c**) 1:2; (**d**) 1:3.

Table 4. Atomic percentages of the elements present in the surfaces of carbonaceous materials with different biochar-to-KOH ratios.

Ratios	Atomic Percentages			
	C	**O**	**N**	**Si**
1:1	80.0	16.6	1.1	2.3
1:2	73.1	22.4	1.1	3.4
1:3	70.7	24.2	0.9	4.2

The C(1s) XPS spectra of the resultant HAC are shown in Figure 7b–d with the four most prominent deconvoluted components of the C(1s) envelope shown in each panel. Relative contents of carbon species present in HACs based on the XPS survey spectra are presented in Table 5. The binding energy of 284.5 eV is attributed to the C–C, C=C, and C–H bonds. Moreover, the binding energies of 286.4 eV, 287.8 eV, and 289.1 eV are typically assigned to the C–OH, C=O, and O=C–OH functional groups, respectively [48]. Deconvolution of all the C(1s) spectra resulted in a main peak located at 284.4 eV, corresponding to the C–C, C=C, and C–H bonds. In Figure 7b–d, deconvolution of the C(1s) peak of the HAC resulted in three peaks located at binding energies of 286.4 eV, 287.8 eV, and 289.1 eV, which are attributed to the C–OH, C=O, and O=C–OH functional groups, respectively. Usually, the C(1s) XPS spectrum of commercial activated carbon shows four similar components that correspond to carbon

atoms in different functional groups: the non-oxygenated C at 284.5 eV for C=C/C–C in aromatic rings, the C in C–O bonds at 286.4 eV for epoxy and alkoxy, the carbonyl C at 287.8 eV for C=O, and the carboxylate carbon at 289.1 eV for O–C=O [49]. Relative percentages of oxygenated functional groups increase with increasing biochar-to-KOH ratios, whereas the nonoxygenated functional group slightly decreases (Table 5). The values obtained in Table 5 for HAC samples are comparable with the values for several commercial activated charcoals such as Superchar, Darco KB-B, Norit B Supra, and Norit U.S.P. XX [50].

Table 5. Relative contents of carbon species present in the carbonaceous materials based on XPS survey spectra.

Samples	Ratios	Percentages of Relative Content			
		C–C/C=C	C–O	C=O	O–C=O
HAC	1:1	78.3	10.3	5.4	6.0
	1:2	76.1	11.2	5.9	6.8
	1:3	75.1	12.2	6.5	6.2
SuperChar	-	73.4	15.7	5.7	5.1
Darco KB-B	-	78.1	12.8	6.2	2.9
Norit B Supra	-	78.6	15.1	2.6	3.7
Norit U.S.P. XX	-	84.9	8.8	3.2	3.1

TG-DTA (Thermogravimetric and differential thermal analysis) of HAC under nitrogen atmosphere was investigated for thermal stability, which is shown in Figure 8. An approximately 20 wt % mass loss was detected when the material was heated up to 1000 °C. Derivative weight loss curves showed that the loss was occurred at <200 °C, which was attributed to the loss of absorbed moisture.
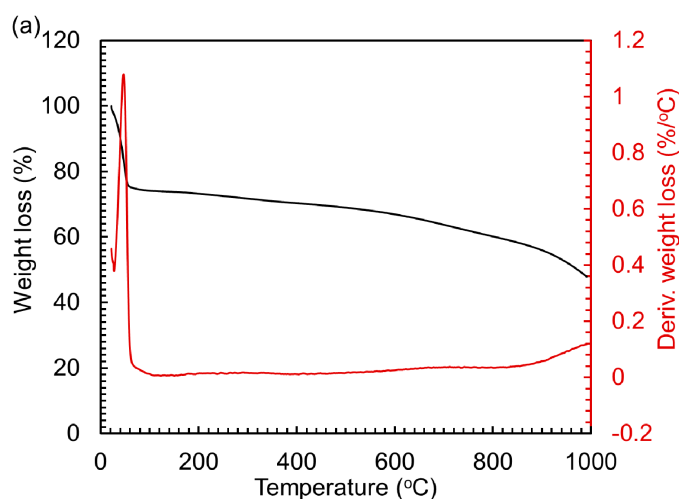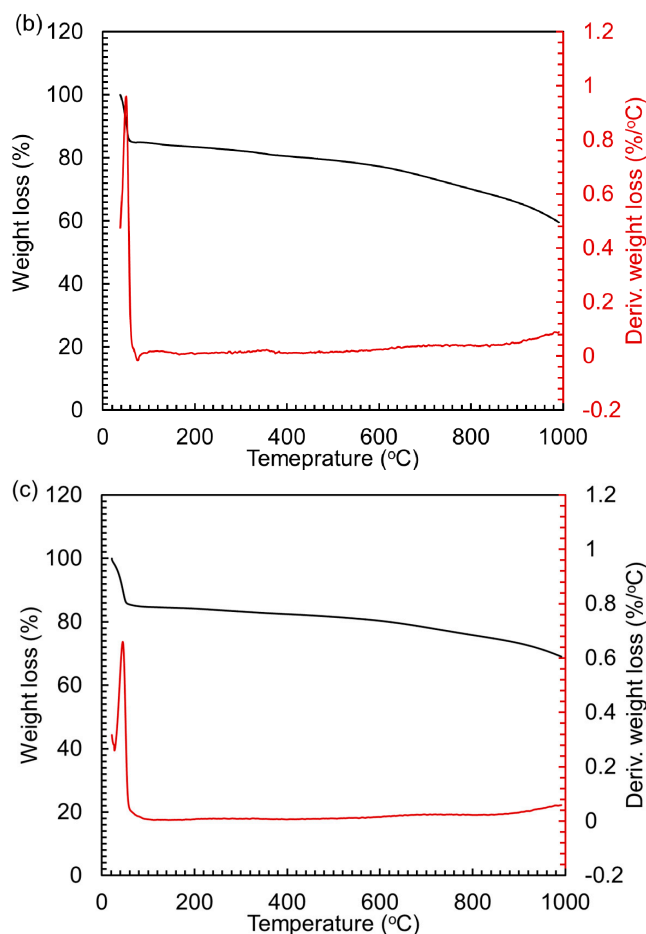

Figure 8. *Cont.*

Figure 8. TG-DTA (Thermogravimetric and differential thermal analysis) curves for hemp-derived activated carbon obtained using different ratios of biochar to KOH ((**a**) 1:1, (**b**) 1:2, and (**c**) 1:3).

Oxygenated functional groups in the surface of carbon material are presumed to be the main active sites. HAC has oxygenated surface functional groups and high thermal stability, so can be used as catalysts for high-temperature applications such as pyrolysis, gasification, hydrodeoxygenation, or decarboxylation processes.

As shown above, both KOH and NaOH provide high-surface-area activated carbon from hemp fiber biochar. Both KOH and NaOH are believed to act as dehydrating agents which influence the pyrolytic decomposition and inhibit the formation of tar, thus enhancing the yield of carbon. Impregnation of KOH into the biochar first results in degradation of the cellulosic material and then carbonization, leading to dehydration that results in charring and aromatization of the carbon skeleton and creation of the porous structure [51]. A pore structure with resultant high surface area is formed by the rigorous evolution of gaseous by-products during KOH activation. According to the chemical activation mechanism [52,53], it is suggested that during activation, the chemical reaction between KOH and carbon proceeds as $6KOH + 2C = 2K + 3H_2 + 2K_2CO_3$; followed by either decomposition of K_2CO_3 or reaction of $K/K_2CO_3/CO_2$ with carbon, the production of H_2 will potentially open up the pores. More importantly, according to Viculis et al. [54], potassium might play an important role in greatly increasing the surface area. The produced potassium atoms form an intercalation compound, KC_8. Upon treatment with water after activation, the reaction between potassium intercalated compounds and aqueous solvent opens up the pores [54]. As shown in Table 1, it was found that with increased KOH loading in the activation reaction, the surface area of the resulting product increased, being consistent with this mechanism.

4. Conclusions

➢ Hemp-fiber-derived highly mesoporous activated carbon (HAC) with large surface area and pore volume was synthesized.

➢ The final product was found to be insensitive to the synthesis temperature of the intermediate product (biochar).

➢ Surface morphologies of HAC were confirmed using several physicochemical techniques such as BET, SEM, TEM, XRD, FTIR, Raman, and XPS analysis.

References

1. Jain, A.; Balasubramanian, R.; Srinivasan, M. Hydrothermal conversion of biomass waste to activated carbon with high porosity: A review. *Chem. Eng. J.* **2016**, *283*, 789–805. [CrossRef]

2. Li, X.; Liu, S.; Huang, Y.; Zheng, Y.; Harper, D.P.; Zheng, Z. Preparation and Foaming Mechanism of Pyrocarbon Foams Controlled by Activated Carbon as the Transplantation Core. *ACS Sustain. Chem. Eng.* **2018**, *6*, 3515–3524. [CrossRef]

3. Kim, M.-H.; Kim, K.-B.; Park, S.-M.; Roh, K.C. Hierarchically structured activated carbon for ultracapacitors. *Sci. Rep.* **2016**, *6*, 21182. [CrossRef] [PubMed]

4. Ba, H.; Wang, W.; Pronkin, S.; Romero, T.; Baaziz, W.; Nguyen-Dinh, L.; Chu, W.; Ersen, O.; Pham-Huu, C. Biosourced Foam-Like Activated Carbon Materials as High-Performance Supercapacitors. *Adv. Sustain. Syst.* **2018**, *2*. [CrossRef]

5. Bansal, R.; Donnet, J.; Stoeckli, F. *Active Carbon*; Marcell Dekker: New York, NY, USA, 1988.

6. Bardestani, R.; Kaliaguine, S. Steam activation and mild air oxidation of vacuum pyrolysis biochar. *Biomass Bioenergy* **2018**, *108*, 101–112. [CrossRef]

7. Tay, T.; Ucar, S.; Karagöz, S. Preparation and characterization of activated carbon from waste biomass. *J. Hazard. Mater.* **2009**, *165*, 481–485. [CrossRef] [PubMed]

8. Li, S.; Han, K.; Li, J.; Li, M.; Lu, C. Preparation and characterization of super activated carbon produced from gulfweed by KOH activation. *Microporous Mesoporous Mater.* **2017**, *243*, 291–300. [CrossRef]

9. Afdhol, M.; Amiliana, R.; Hanafi, A. Preparation of Activated Carbon from Palm Shells Using KOH and ZnC$_{l2}$ as the Activating Agent. In Proceedings of the IOP Conference Series: Earth and Environmental Science, Iasi, Romania, 17–18 May 2018.

10. Hemp Fibres Better Than Graphene. Available online: http://www.bbc.com/news/science-environment-28770876 (accessed on 19 April 2018).

11. Wang, H.; Xu, Z.; Kohandehghan, A.; Li, Z.; Cui, K.; Tan, X.; Stephenson, T.; King'ondu, C.K.; Holt, C.M.B.; Olsen, B.C.; et al. Interconnected Carbon Nanosheets Derived from Hemp for Ultrafast Supercapacitors with High Energy. *ACS Nano* **2013**, *7*, 5131–5141. [CrossRef] [PubMed]

12. Yang, R.; Liu, G.; Xu, X.; Li, M.; Zhang, J.; Hao, X. Surface texture, chemistry and adsorption properties of acid blue 9 of hemp (*Cannabis sativa* L.) bast-based activated carbon fibers prepared by phosphoric acid activation. *Biomass Bioenergy* **2011**, *35*, 437–445. [CrossRef]

13. Rosas, J.; Bedia, J.; Rodríguez-Mirasol, J.; Cordero, T. HEMP-derived activated carbon fibers by chemical activation with phosphoric acid. *Fuel* **2009**, *88*, 19–26. [CrossRef]

14. Subramanian, V.; Luo, C.; Stephan, A.; Nahm, K.; Thomas, S.; Wei, B. Supercapacitors from activated carbon derived from banana fibers. *J. Phys. Chem. C* **2007**, *111*, 7527–7531. [CrossRef]

15. Roman, S.; Nabais, J.V.; Ledesma, B.; González, J.; Laginhas, C.; Titirici, M. Production of low-cost adsorbents with tunable surface chemistry by conjunction of hydrothermal carbonization and activation processes. *Microporous Mesoporous Mater.* **2013**, *165*, 127–133. [CrossRef]

16. Liu, Z.; Zhang, F.-S. Removal of copper(II) and phenol from aqueous solution using porous carbons derived from hydrothermal chars. *Desalination* **2011**, *267*, 101–106. [CrossRef]

17. White, R.J.; Yoshizawa, N.; Antonietti, M.; Titirici, M.-M. A sustainable synthesis of nitrogen-doped carbon aerogels. *Green Chem.* **2011**, *13*, 2428–2434. [CrossRef]

18. Fellinger, T.P.; White, R.J.; Titirici, M.M.; Antonietti, M. Borax-Mediated Formation of Carbon Aerogels from Glucose. *Adv. Funct. Mater.* **2012**, *22*, 3254–3260. [CrossRef]

19. Fernandez, M.; Ledesma, B.; Román, S.; Bonelli, P.; Cukierman, A. Development and characterization of activated hydrochars from orange peels as potential adsorbents for emerging organic contaminants. *Bioresour. Technol.* **2015**, *183*, 221–228. [CrossRef] [PubMed]

20. Gao, F.; Shao, G.; Qu, J.; Lv, S.; Li, Y.; Wu, M. Tailoring of porous and nitrogen-rich carbons derived from hydrochar for high-performance supercapacitor electrodes. *Electrochim. Acta* **2015**, *155*, 201–208. [CrossRef]

21. Islam, M.A.; Tan, I.; Benhouria, A.; Asif, M.; Hameed, B. Mesoporous and adsorptive properties of palm date seed activated carbon prepared via sequential hydrothermal carbonization and sodium hydroxide activation. *Chem. Eng. J.* **2015**, *270*, 187–195. [CrossRef]

22. Zhu, X.; Liu, Y.; Qian, F.; Zhou, C.; Zhang, S.; Chen, J. Role of hydrochar properties on the porosity of hydrochar-based porous carbon for their sustainable application. *ACS Sustain. Chem. Eng.* **2015**, *3*, 833–840. [CrossRef]

23. Ding, L.; Zou, B.; Li, Y.; Liu, H.; Wang, Z.; Zhao, C.; Su, Y.; Guo, Y. The production of hydrochar-based hierarchical porous carbons for use as electrochemical supercapacitor electrode materials. *Coll. Surf. A Physicochem. Eng. Asp.* **2013**, *423*, 104–111. [CrossRef]

24. Unur, E.; Brutti, S.; Panero, S.; Scrosati, B. Nanoporous carbons from hydrothermally treated biomass as anode materials for lithium ion batteries. *Microporous Mesoporous Mater.* **2013**, *174*, 25–33. [CrossRef]

25. Gong, Y.; Wang, H.; Wei, Z.; Xie, L.; Wang, Y. An efficient way to introduce hierarchical structure into biomass-based hydrothermal carbonaceous materials. *ACS Sustain. Chem. Eng.* **2014**, *2*, 2435–2441. [CrossRef]

26. Romero-Anaya, A.J.; Ouzzine, M.; Lillo-Ródenas, M.; Linares-Solano, A. Spherical carbons: Synthesis, characterization and activation processes. *Carbon* **2014**, *68*, 296–307. [CrossRef]

27. Sevilla, M.; Fuertes, A.B. Sustainable porous carbons with a superior performance for CO_2 capture. *Energy Environ. Sci.* **2011**, *4*, 1765–1771. [CrossRef]

28. Falco, C.; Marco-Lozar, J.P.; Salinas-Torres, D.; Morallon, E.; Cazorla-Amorós, D.; Titirici, M.-M.; Lozano-Castelló, D. Tailoring the porosity of chemically activated hydrothermal carbons: Influence of the precursor and hydrothermal carbonization temperature. *Carbon* **2013**, *62*, 346–355. [CrossRef]

29. Sevilla, M.; Fuertes, A.; Mokaya, R. High density hydrogen storage in superactivated carbons from hydrothermally carbonized renewable organic materials. *Energy Environ. Sci.* **2011**, *4*, 1400–1410. [CrossRef]

30. Falco, C.; Sieben, J.M.; Brun, N.; Sevilla, M.; Van der Mauelen, T.; Morallón, E.; Cazorla-Amorós, D.; Titirici, M.M. Hydrothermal Carbons from Hemicellulose-Derived Aqueous Hydrolysis Products as Electrode Materials for Supercapacitors. *ChemSusChem* **2013**, *6*, 374–382. [CrossRef] [PubMed]

31. Yang, S.-Y.; Chang, K.-H.; Huang, Y.-L.; Lee, Y.-F.; Tien, H.-W.; Li, S.-M.; Lee, Y.-H.; Liu, C.-H.; Ma, C.-C.M.; Hu, C.-C. A powerful approach to fabricate nitrogen-doped graphene sheets with high specific surface area. *Electrochem. Commun.* **2012**, *14*, 39–42. [CrossRef]

32. Islam, M.A.; Ahmed, M.; Khanday, W.; Asif, M.; Hameed, B. Mesoporous activated carbon prepared from NaOH activation of rattan (*Lacosperma secundiflorum*) hydrochar for methylene blue removal. *Ecotoxicol. Environ. Saf.* **2017**, *138*, 279–285. [CrossRef] [PubMed]

33. Foo, K.; Hameed, B. Preparation and characterization of activated carbon from pistachio nut shells via microwave-induced chemical activation. *Biomass Bioenergy* **2011**, *35*, 3257–3261. [CrossRef]

34. Foo, K.; Hameed, B. Utilization of rice husks as a feedstock for preparation of activated carbon by microwave induced KOH and K_2CO_3 activation. *Bioresour. Technol.* **2011**, *102*, 9814–9817. [CrossRef] [PubMed]

35. Lu, Y.; Zhang, S.; Yin, J.; Bai, C.; Zhang, J.; Li, Y.; Yang, Y.; Ge, Z.; Zhang, M.; Wei, L. Mesoporous activated carbon materials with ultrahigh mesopore volume and effective specific surface area for high performance supercapacitors. *Carbon* **2017**, *124*, 64–71. [CrossRef]

36. Zhao, D.; Feng, J.; Huo, Q.; Melosh, N.; Fredrickson, G.H.; Chmelka, B.F.; Stucky, G.D. Triblock copolymer syntheses of mesoporous silica with periodic 50 to 300 angstrom pores. *Science* **1998**, *279*, 548–552. [CrossRef] [PubMed]

37. Zou, L.; Li, L.; Song, H.; Morris, G. Using mesoporous carbon electrodes for brackish water desalination. *Water Res.* **2008**, *42*, 2340–2348. [CrossRef] [PubMed]

38. Suganuma, S.; Nakajima, K.; Kitano, M.; Yamaguchi, D.; Kato, H.; Hayashi, S.; Hara, M. Hydrolysis of cellulose by amorphous carbon bearing SO_3H, COOH, and OH groups. *J. Am. Chem. Soc.* **2008**, *130*, 12787–12793. [CrossRef] [PubMed]

39. Infraed and Ramn Characteristic Group Frequencies. Available online: https://www.researchgate.net/profile/Muzammil_Iqbal2/post/Authentic_IR_spectral_database/attachment/59d6591679197b80779aebbd/AS:540994395439105@1505994523971/download/Infrared+and+Raman+Characteristic+Group+Frequencies+by+George+Socrates.pdf (accessed on 19 April 2018).

40. Barkauskas, J.; Dervinyte, M. Investigation of the functional groups on the surface of activated carbons. *J. Serbian Chem. Soc.* **2004**, *69*, 363–375. [CrossRef]

41. Reina, A.; Jia, X.; Ho, J.; Nezich, D.; Son, H.; Bulovic, V.; Dresselhaus, M.S.; Kong, J. Large area, few-layer graphene films on arbitrary substrates by chemical vapor deposition. *Nano Lett.* **2008**, *9*, 30–35. [CrossRef] [PubMed]

42. Liu, Y.; Zhao, Y.; Li, K.; Wang, Z.; Tian, P.; Liu, D.; Yang, T.; Wang, J. Activated carbon derived from chitosan as air cathode catalyst for high performance in microbial fuel cells. *J. Power Sources* **2018**, *378*, 1–9. [CrossRef]

43. Xu, S.; Yong, L.; Wu, P. One-pot, green, rapid synthesis of flowerlike gold nanoparticles/reduced graphene oxide composite with regenerated silk fibroin as efficient oxygen reduction electrocatalysts. *ACS Appl. Mater. Interfaces* **2013**, *5*, 654–662. [CrossRef] [PubMed]

44. Maslova, O.; Ammar, M.; Guimbretière, G.; Rouzaud, J.-N.; Simon, P. Determination of crystallite size in polished graphitized carbon by Raman spectroscopy. *Phys. Rev. B* **2012**, *86*. [CrossRef]

45. Matthews, M.; Pimenta, M.; Dresselhaus, G.; Dresselhaus, M.; Endo, M. Origin of dispersive effects of the Raman D band in carbon materials. *Phys. Rev. B* **1999**, *59*. [CrossRef]

46. Tai, Z.; Zhang, Q.; Liu, Y.; Liu, H.; Dou, S. Activated carbon from the graphite with increased rate capability for the potassium ion battery. *Carbon* **2017**, *123*, 54–61. [CrossRef]

47. Keeping, M.; Reynolds, O. Silicon in agriculture: New insights, new significance and growing application. *Ann. Appl. Biol.* **2009**, *155*. [CrossRef]

48. Yang, D.; Velamakanni, A.; Bozoklu, G.; Park, S.; Stoller, M.; Piner, R.D.; Stankovich, S.; Jung, I.; Field, D.A.; Ventrice, C.A. Chemical analysis of graphene oxide films after heat and chemical treatments by X-ray photoelectron and Micro-Raman spectroscopy. *Carbon* **2009**, *47*, 145–152. [CrossRef]

49. Seah, M. The quantitative analysis of surfaces by XPS: A review. *Surf. Interface Anal.* **1980**, *2*, 222–239. [CrossRef]

50. Burke, G.M.; Wurster, D.E.; Berg, M.J.; Veng-Pedersen, P.; Schottelius, D.D. Surface characterization of activated charcoal by X-ray photoelectron spectroscopy (XPS): Correlation with phenobarbital adsorption data. *Pharm. Res.* **1992**, *9*, 126–130. [CrossRef] [PubMed]

51. Smíšek, M.; Černý, S. *Active Carbon: Manufacture, Properties and Applications*; Elsevier Publishing Company: New York, NY, USA, 1970; Volume 12.

52. Lillo-Ródenas, M.; Cazorla-Amorós, D.; Linares-Solano, A. Understanding chemical reactions between carbons and NaOH and KOH: An insight into the chemical activation mechanism. *Carbon* **2003**, *41*, 267–275. [CrossRef]

53. Lillo-Ródenas, M.; Juan-Juan, J.; Cazorla-Amorós, D.; Linares-Solano, A. About reactions occurring during chemical activation with hydroxides. *Carbon* **2004**, *42*, 1371–1375. [CrossRef]

54. Viculis, L.M.; Mack, J.J.; Kaner, R.B. A chemical route to carbon nanoscrolls. *Science* **2003**, *299*, 1361. [CrossRef] [PubMed]